

Realization of discretized response in rare-earth vanadates accessed by AC susceptibility and magnetocaloric methods

Yuntian Li,^{1,2} Linda Ye,^{1,2} Mark P. Zic,^{2,3} Matthias S. Ikeda,^{1,2} Arkady Shekhter,⁴ and Ian R. Fisher^{1,2}

¹*Department of Applied Physics, Stanford University, Stanford, California 94305, USA*

²*Geballe Laboratory for Advanced Materials, Stanford University, Stanford, California 94305, USA*

³*Department of Physics, Stanford University, Stanford, California 94305, USA*

⁴*Los Alamos National Laboratory, Los Alamos, New Mexico 87545, USA*

(Dated: March 7, 2025)

This report presents a new technique to probe the quantitative dynamical response of the magnetic field induced heating/cooling process in rare-earth vanadium materials. The approach combines AC susceptibility and AC caloric measurements to reveal the intrinsic timescale associated with the magnetic relaxation process of rare-earth ions at low temperatures. Utilizing the well-known crystal field effect in YbVO_4 , we prove and demonstrate a discretized thermal analysis through a common spin-lattice relaxation phenomenon. The demonstration experiment presented in this study provides a general approach to quantitatively address multiple measured quantities in one unified discretized thermal circuit analysis. It can be extended to study other magnetic, dielectric, and elastic materials exhibiting a complex response to an external driving field in the presence of intrinsic interactions and fluctuations, particularly when an energy dissipation process is within an accessible frequency regime.

I. Introduction

The method of AC susceptometry (χ^{ac}) is widely adopted for studying the dynamical magnetic response of newly-discovered materials [1]. The technique has proven to be a useful tool to characterize a wide variety of phase transitions in a wide variety of materials, including extended solids, molecular magnets, and disordered magnetic systems. It eventually led to the successful commercialization of the AC magnetometer devices [2] that are now utilized extensively in many research facilities. When deriving a dynamical response χ^{ac} , it is typically assumed that the thermodynamic state of a magnetic system is between the adiabatic and isothermal regimes, leading to some characteristic frequency dependence [1, 3]. However, despite the prevalent use of χ^{ac} in discovering new magnetic phenomena, magnetic and thermal properties are usually discussed separately and the actual experimental thermal condition is often overlooked. Without knowing the associated caloric processes, the cause of magnetization dynamics remains speculative due to the inability to distinguish between intrinsic and measurement-specific factors, often leaving the quantitative relaxation characteristics of χ^{ac} poorly defined in many new magnetic materials [4].

To better understand the thermal conditions of materials in the presence of a driving field, common engineering methods, such as finite element simulations, computational fluid dynamics [5], and thermal imaging [6] primarily focus on characterizing heat flow based on well-established thermal constants and geometric effects. Such simulations require well-defined boundary conditions of heat sources as well. If, however, a material substance demonstrates a complex magnetic response and caloric effect due to an unknown internal process, the efficacy of any simulation methods is significantly reduced.

Motivated by characterizing new magnetic materials that exhibit complex magneto-thermal responses, we introduce a discretized thermal analog circuit approach to extend the analysis of the magnetocaloric effect (MCE) into the frequency domain. The MCE refers to the temperature change in a material that responds to variations in an external magnetic field [7, 8]. From a first-principle thermodynamic description, the MCE has been extensively studied and applied in various fields, such as adiabatic demagnetization refrigeration techniques [9] and characterizing the order of phase transitions [10, 11]. The dominant method that is typically used to make MCE measurements is in the time domain, in response to a swept magnetic field (see, for example, [8]). While several previous studies attempted to measure the MCE in periodically changing fields (i.e. an AC, or dynamic, MCE) [12, 13], quantitative analysis of a thermal transfer function is usually limited by choice of materials and temperature regime [14, 15], and to date a formal analysis has not been available.

When magnetic fields do work with a system of magnetic species, both magnetization and the temperature of the material develop a non-instantaneous response. To quantitatively describe the existence of internal magnetic dynamics within an AC calorimetry method, we first define a set of generalized response functions $\alpha(\omega)$ and $\tilde{T}(\omega)$ that describe the overall dynamical magnetic moment and temperature response under a driven magnetic field $\Delta H = h \sin(\omega t)$. We use the complex representation of the sinusoidal function and represent ΔH as $ihe^{-i\omega t}$ (the notion of complex representation implies that negative ω is omitted). The magnetization M and temperature T are:

$$\begin{aligned} M &= M^{dc} - ihe^{-i\omega t}\alpha(\omega) \\ T &= T_0 - ihe^{-i\omega t}\gamma h\tilde{T}(\omega) \end{aligned} \quad (1)$$

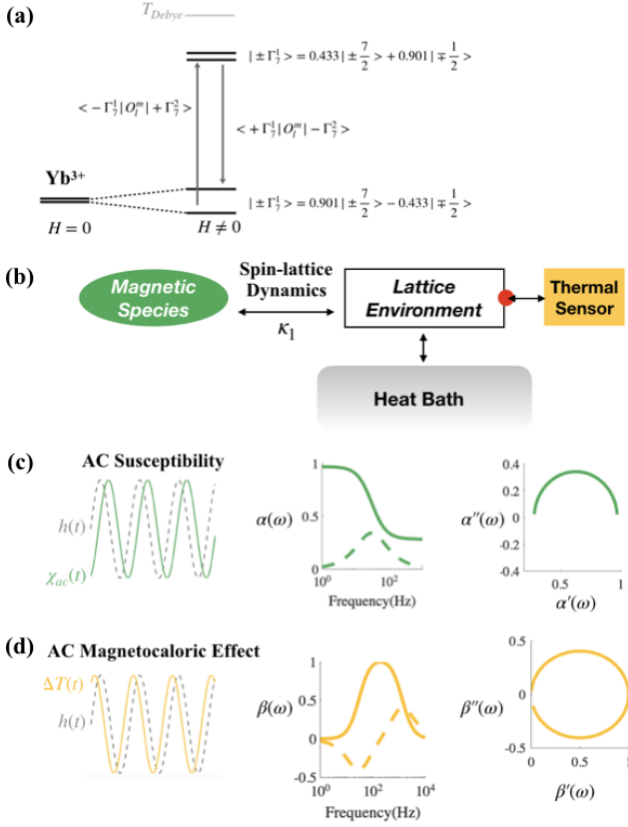


FIG. 1. (a) Schematics of crystal electric field levels and indirect transition corresponding to Yb^{3+} ion embedded in the RVO_4 crystal field environment. The lower two levels represent Kramers ground-state doublets, which undergo splitting when an external magnetic field is along the c -axis. The higher states correspond to the second excited states of the crystal field levels. (b) Discretized spin-lattice thermal circuit model components that are summarized from the experimental observations, highlighting the major time constant measured by frequency-dependent AC techniques caused by the indirect transition of the ground-state doublets. (c,d) Solution of the equivalent circuit of systems based on the internal discretized thermal circuit model. In the left panels, the response signal is plotted to illustrate the phase difference between the time-dependent solution and the signals. In the middle panels, solid lines represent the real components (α' and \tilde{T}'), and dashed lines represent the imaginary components (α'' and \tilde{T}''). In the right panels, the real components of each solution are plotted against their respective imaginary parts in a Cole-Cole plot. This representation maintains a fixed aspect ratio of 1:1 for the x and y axes.

where both α and \tilde{T} are complex response functions

$$\begin{aligned}\alpha &= \alpha' + i\alpha'' \\ \tilde{T} &= \tilde{T}' + i\tilde{T}''\end{aligned}\quad (2)$$

and where M and T represent the experimentally accessible thermodynamic states. M^{dc} and $\chi^{dc} = \frac{dM^{dc}}{dH}$ are the static magnetization and magnetic susceptibility determined by the equilibrium condition. T_0 is the con-

stant background temperature of the bath. As illustrated in Fig. 1(b), when the insulator sample is composed of a $4f$ magnetic species (spin) and a crystal environment (lattice), the spin-lattice relaxation rate τ between the two internal degrees of freedom characterizes the energy dissipation. In a common case when the dissipation rate is sufficiently high and characterized by the microscopic motion of magnetic spins and lattice vibrations (i.e. κ_1 is large), the spin and lattice have the same temperature, and the experimentally observed time constant characterizes heat flow between the sample and its environment. If, however, the exchange rate is limited, the energy dissipation process between spin and lattice must imply that the temperature of the magnetic species (T^{4f}) and the lattice ($T^{lattice}$) are different, and of course that both can be different to T_0 . Taking reference from parameters of DC thermal conductivity measurements, the heat diffusion across the entire sample is uniform (see Appendix. E). Moreover, we assume for simplicity that the spins themselves are in equilibrium, since they are able to exchange energy via dipolar and exchange interactions. Thus, we can define a separate effective temperature for the spin system (T^{4f}) that is nevertheless distinct from that of the lattice. Such an effect is, by definition, distinct from the extrinsic heat flow, which can be observed by a separate time constant in the experiment.

The major finding of this report is summarized in Fig. 1(c,d), where the two response functions $\alpha(\omega)$ and $\tilde{T}(\omega)$ can be solved analytically from a physically equivalent thermal circuit model, and can be measured experimentally.

YbVO_4 is an ideal model material system to justify the proposed experimental principle outlined above. This is because its low-temperature properties are completely described by a simple pseudo-spin 1/2 Kramers doublet that is well-separated from and (under the influence of perturbing fields) interacts weakly with higher excited states. The moments interact principally via dipolar interactions, leading to an antiferromagnetic state below a Neel temperature of approximately 93 mK[16]. A large magnetic and magnetocaloric response associated with entropy changes can be anticipated and experimentally obtained in the paramagnetic state [17, 18].

Under an applied magnetic field along the easy c -axis of the crystal direction, the Kramers ground state doublet degeneracy of the Yb ions in YbVO_4 is split. If this is done adiabatically, the system is no longer in equilibrium and must relax. Spin-lattice relaxation occurs by transitions between the distinct Crystal Electric Field (CEF) magnetic states and is either direct (involving a single phonon) or indirect (the transition **blue** involves a third or more intermediate states and two or more phonons). For Yb ions in YbVO_4 , direct transitions are not allowed by symmetry (see Appendix. B), and the ion can only relax by indirect processes (Fig. 1(a)). Zeeman splitting of the CEF eigenstates necessarily leads to a strong field dependence on the associated relaxation rates, making this an especially useful material system to identify internal

relaxation effects.

At a temperature much lower than the Debye temperature, very few phonons are available to participate in the dynamics, resulting in a slow magnetic response due to the low transition probability; a manifestation of the phonon bottleneck effect. The indirect transition effectively decouples the material into a separate bath of spins and a bath of phonons, resulting in large internal time constants that describe the non-instantaneous relaxation behavior. The associated slow relaxation effects in rare-earth compounds that exhibit large magnetic anisotropies have been understood since the 1960s [19]. The well-defined magnetic properties of YbVO_4 imply that the proposed AC MCE approach can be confirmed experimentally in this system.

Based on the well-defined and large magnetocaloric effect of YbVO_4 , we perform a combination of χ^{ac} and AC MCE measurements as a set of reciprocal approaches to measure the internal time constant associated with the spin-lattice relaxation rate based on the thermodynamic response of the material. As shown in Fig. 1(b), the measured heat conduction rate κ_1 can be dynamically described by an effective spin-lattice energy exchange thanks to the indirect transition process between the ground state doublet and its well-separated excited states. κ_1 obtained from a caloric effect is different from the lattice thermal conductivity in a thermal transport or susceptibility measurement (see Appendix. E). In the following sections, we discuss the relevant experimental techniques established by measuring the AC MCE of YbVO_4 .

II. Experimental methods

Single crystals of YbVO_4 and GdVO_4 were synthesized via slow cooling in a flux of $\text{Pb}_2\text{V}_2\text{O}_7$ using a mixture of high purity rare-earth oxides precursors, Yb_2O_3 (99.99% purity from Alfa Aesar, CAS Number: 1314-37-0) and Gd_2O_3 (99.99% purity from Alfa Aesar, CAS Number: 12064-62-9). More details related to the flux-growth synthesis method can be found in Refs. [20–22].

AC susceptibility measurements were performed in a Quantum Design Magnetic Property Measurement System (MPMS) with the AC susceptometer measurement options. The technique and procedure of the measurement techniques can be found elsewhere [1].

AC MCE was performed using a customized probe within the same MPMS, ensuring a direct comparison of the two techniques can be made. The MCE measurement device consists of a polished sample material with a thickness between 30-100 μm , a thermometer attached to the top surface of the sample, and a quartz sample holder that is thermally anchored to the bottom surface of the sample. The thermoresistor attached to the sample is connected with a Wheatstone resistance bridge that is anchored to the heat bath (located on the part of the probe far apart from the measured material).

More details on the materials for the device fabrication, data analysis, heat transfer, and thermodynamic consideration can be found in the following text and Appendix sections.

The data analysis in this work is performed with the nonlinear least-squares fitting method.

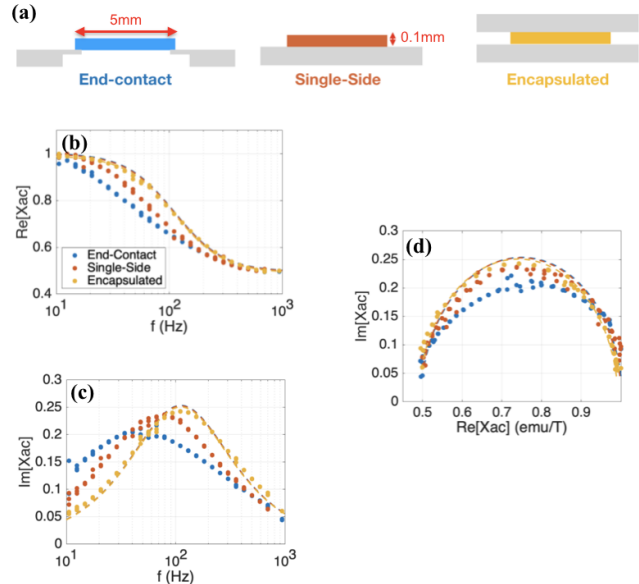


FIG. 2. Data illustrating how sample mounting configurations can affect AC Magnetic relaxation. Panel (a) illustrates three different sample mounting configurations, described in the main text. Colored bars represent the sample that is to be measured, together with its dimensions. The same sample of YbVO_4 is used for all three configurations to enable direct comparison. Grey blocks indicate quartz platforms that serve as heat baths. The sample is oriented with the magnetic field aligned along the long c -axis of the crystal (horizontal in the schematic diagrams). AC susceptibility measurements were made at 3 K, 0.2 T, using an AC field of 3 Oe. Panels (b) and (c) show the real and imaginary parts of χ^{ac} , $\text{Re}[\chi^{ac}]$ and $\text{Im}[\chi^{ac}]$ respectively. Panel (c) shows the associated Cole-Cole plot in which frequency is an implicit variable. Data are shown for the three mounting configurations indicated in panel (a), using the same colors to differentiate the three configurations. Dashed lines in (b,c,d) are fit results based on Eq.3. The encapsulated configuration (yellow data points) yields data that are closest to the idealized Debye relaxation conditions.

III. Single- τ Debye relaxation observed in χ^{ac} under experimental quasi-adiabatic conditions

We first examine the AC susceptibility of a single crystal of YbVO_4 , with the aim of demonstrating an important point, namely that the measured susceptibility can depend strongly on the experimental configurations that are used, even when internal relaxation processes dominate the quasi-adiabatic response.

When a single relaxation time τ governs the periodic flow of energy in a system, as is anticipated for YbVO₄ due to the phonon bottleneck effect described above, the dynamical susceptibility as a function of driven frequency ω is given by the Debye relaxation process:

$$\begin{aligned}\chi(\omega) &= \chi_S + \frac{\chi_0 - \chi_S}{1 + i\omega\tau} \\ &= \chi_0 - \frac{\chi_0 - \chi_S}{1 + \frac{i}{\omega\tau}}\end{aligned}\quad (3)$$

where χ_0 and χ_S represent the isothermal susceptibility and adiabatic susceptibility respectively.

To illustrate the effects of extrinsic factors, we first compare the magnetic relaxation behavior of YbVO₄ samples measured in different mounting configurations in Fig. 2, where the same sample mounted in different conditions are listed in Fig. 2 (a). In the first case of end-contact (blue), the sample's extrinsic thermal contact is minimized on both ends using GE Low-Temperature Varnish (GE Varnish) and Teflon materials with relatively low thermal conductivity at low temperatures. In the second case of the single-side mounting condition (red), the sample has one side connected to the sample holder via GE Varnish. This is consistent with the standard procedure recommended by the MPMS system vendor. In the third case, the extrinsic thermal contact is maximized by encapsulating the sample between two quartz surfaces (yellow). Fig. 2(b,c) plots the magnetic relaxation behaviors from χ^{ac} .

A comparison of the measured susceptibility for the three different extrinsic mounting conditions reveals that the adiabatic (high frequency limit) and isothermal (low frequency limit) susceptibility are both independent of the extrinsic condition. Similarly, the magnitude of the excitation field does not affect the adiabatic and isothermal response (we varied the amplitude of the driven field between 1 Oe and 10 Oe, finding that this did not affect the result). This is in contrast with expectations if the relaxation is dominated by external relaxation. Moreover, a single- τ Debye relaxation gives the best fit to experimental data in the encapsulated mounting condition in Fig. 2, when the sample is optimally thermalized to the bath (yellow data points).

To further visualize the relaxation behavior, the real part of the χ^{ac} is plotted against its imaginary part (known as Cole-Cole plot) in Fig. 2(c). Here, we observe that the measurement under good thermal conditions gives an undistorted semicircle with an aspect ratio of 1, while the other two cases slightly deviate from an undistorted circle. The result implies that optimized thermal condition with a uniform thermal contact enables us to further conduct quantitative analysis on the magnetic relaxation behavior of the YbVO₄. Conversely, poor thermal contact, which results in magnetization and temperature oscillations that are more spatially and temporally inhomogeneous, leads to a more complex signature that does not easily reflect the actual quasi-adiabatic

response of the material.

Heat exchange between the magnetic system and its environment is neither temporally instantaneous nor spatially homogeneous for realistic mounting conditions. Consequently, the characteristic time and amount of the heat exchange and associated magnetic relaxation are influenced by both the driven excitation field and the extrinsic mounting conditions, causing the time-dependent magnetic relaxation behavior to not be described by a uniform thermodynamic character. Moreover, when an internal process exists, the thermodynamic condition of each subsystem has to be described separately, making the overall quasi-adiabatic response unknown.

The above insight indicates that the thermal response of a material cannot, and indeed must not, be neglected in the measurement of the AC magnetic response. This motivates a more careful theoretical description and experimental investigation of the cross-relaxation that occurs in response to dynamic excitation.

IV. Cross-relaxation in dynamical susceptibility

Although the single- τ relaxation behavior described above is dominated by a spin-lattice relaxation rate in YbVO₄, we emphasize that intermixing of intrinsic and extrinsic relaxation processes, particularly when a sample has poor thermal contact with the bath, means that extracting the intrinsic dynamical response of a material can be much more complex than is usually appreciated. In particular, we emphasize that magnetocaloric effects cannot be neglected. In this section, we analyze the χ^{ac} as a response function to assist in understanding the internal magnetic relaxation behavior observed in YbVO₄ and model the process based on thermal circuit analysis methods.

To establish an AC thermal model that captures the Debye relaxation associated with thermodynamic quantities, and which includes magnetocaloric effects, we consider the change of entropy of the magnetic species, ΔS^{4f} , induced by the alternating magnetic field with frequency ω .

Under adiabatic conditions, the total change of free energy of the material is given by $\Delta F_{4f} = -S_{4f}\Delta T^{4f} - M\Delta H$ (i.e. assuming that the free energy of the lattice has negligible field-dependence). In the linear response regime, the cross-relaxation between thermodynamic variables can be written by taking the full derivative of dF_{4f} with respect to T and H :

$$\begin{aligned}\Delta S^{4f}(t) &= -\frac{d\Delta F^{4f}}{dT} = \frac{C^{4f}}{T_0}\Delta T^{4f}(t) + \gamma\Delta H(t) \\ \Delta M(t) &= -\frac{d\Delta F^{4f}}{dH} = \gamma\Delta T^{4f}(t) + \chi^{dc}\Delta H(t)\end{aligned}\quad (4)$$

which defines the time-independent constants of the static magnetic susceptibility χ^{dc} , magnetocaloric coefficient γ , and the heat capacity C_{4f} . The value of γ can

be solved explicitly in an adiabatic condition by knowing the entropy (see Appendix. C), but the value of γ cannot be fixed under a non-adiabatic condition. The steady-state $\Delta H(t)$, $\Delta S^{4f}(t)$ and $\Delta M(t)$ can be represented in the complex frequency space as:

$$\begin{aligned}\Delta H(t) &= -ihe^{-i\omega t} \\ \Delta S^{4f}(t) &= \Delta S^{4f}(\omega)e^{-i\omega t} \\ \Delta M(t) &= \Delta M(\omega)e^{-i\omega t}\end{aligned}\quad (5)$$

The dynamical susceptibility is defined as:

$$\chi^{ac}(\omega) = \frac{\Delta M(t)}{\Delta H(t)} \quad (6)$$

The above description does not include heat flow between the magnetic species and the lattice. Eq.4 can also be applied to quasi-adiabatic conditions, in which the spin system and the lattice exchange energy and can be out of equilibrium with each other. We remind readers that the magnetic species, the lattice, and the external bath are described by the separate temperatures T^{4f} , $T^{lattice}$ and T_0 respectively. Initially we neglect extrinsic thermal relaxation (i.e. heat flow from the lattice to the bath). Temperature oscillations in T^{4f} and $T^{lattice}$ are therefore about an initial value of T_0 . By assuming the magnetocaloric effect heats the sample uniformly in ideal thermal conditions (i.e. neglecting the kind of extrinsic effects described in the previous section), the heat transfer between the spin bath and the lattice can be described by a thermal transfer equation:

$$\begin{aligned}q_{4f-lattice} &= \frac{d}{dt}[T_0 S^{4f}(\omega)e^{-i\omega t}] \\ &= -\kappa_l(T^{4f}(\omega) - T^{lattice})e^{-i\omega t}\end{aligned}\quad (7)$$

Solving for Eq.7, we have:

$$-i\omega T_0 S^{4f}(\omega) = -\kappa_l(T^{4f}(\omega) - T^{lattice}) \quad (8)$$

where κ_l is an effective internal thermal conductivity governing heat flow between the magnetic system and the lattice. The solution of Eq.4,5,6 and 8 gives the exact functional form of a Debye-like relaxation with a time constant $\tau = \frac{C^{4f}}{\kappa_l}$ defined by intrinsic properties of the material:

$$\chi^{ac}(\omega) = \chi_0 - \frac{\gamma^2 T_0 / \kappa_l \tau}{1 - \frac{1}{i\omega\tau}} \quad (9)$$

At this stage we have simply recast the standard Debye relaxation picture in terms of microscopic parameters that reflect the intrinsic flow of energy between subsystems of the material (i.e. between the $4f$ moments and the lattice, each of which is modeled as being in equilibrium) at an average temperature T_0 . However, we have done this in a way that naturally accounts for

and includes the magnetocaloric effect in a unified manner. Furthermore, this thermal circuit approach can be extended to include multiple discretized components, including relaxation to the environment.

In the following sections, we develop the full description of the unified magnetocaloric effect in the presence of extrinsic heat flow and application of this analysis to measurements of YbVO_4 to robustly extract intrinsic and external time constants.

V. Quasi-adiabatic magnetocaloric response including relaxation to the environment

In the previous section, in which we neglected external thermal relaxation to the environment, we showed that χ^{ac} follows a single- τ Debye-relaxation. The effect of extrinsic thermal relaxation on the measured χ^{ac} is negligible if it is well separated from the other time constant in the circuit, as is the case for the yellow data shown in Fig. 2. However, the effect of extrinsic thermal relaxation is not negligible for caloric responses because (as we will show below) the frequency-dependence of the caloric response is governed by very different equations for the two observables, M and $T^{lattice}$.

To fully describe the caloric response, we consider the following set of equations that incorporate the $4f$ subsystem, the lattice, and a constant-temperature heat bath:

$$\begin{aligned}S^{4f}(\omega) &= \frac{C^{4f}}{T_0}T^{4f}(\omega) - i\gamma h \\ \Delta M(\omega) &= \gamma T^{4f}(\omega) - i\chi^{dc}h \\ -i\omega T_0 S^{4f}(\omega) &= -\kappa_l(T^{4f}(\omega) - T^{lattice}(\omega)) \\ -i\omega T_0 S^{lattice}(\omega) &= -i\omega C^l T^{lattice}(\omega) \\ &= -\kappa_l(T^{lattice}(\omega) - T^{4f}(\omega)) - \\ &= -\kappa_b(T^{lattice}(\omega) - T_0)\end{aligned}\quad (10)$$

where κ_b is the thermal conductivity describing heat flow between the sample and the thermal bath. Solving Eq. 10 for the oscillation of the lattice temperature $\Delta T^{lattice}(\omega) = T^{lattice}(\omega) - T_0$, we find:

$$\Delta T^{lattice} = \frac{ihT_0\gamma\kappa_l\omega}{i\kappa_l\kappa_b + (C^{4f} + C^l)\kappa_l\omega + C^{4f}\kappa_b\omega - iC^{4f}C^l\omega^2} \quad (11)$$

The real and imaginary parts of this solution are plotted in Fig. 1(c, d). As we show below, these are quantitatively captured by measurements of YbVO_4 . We note that the functional form of the AC MCE also depict a portion of a circular feature in the Cole-Cole plot, similar to the appearance of the χ^{ac} measurement. Looking at the solutions more carefully, the peak in the real part

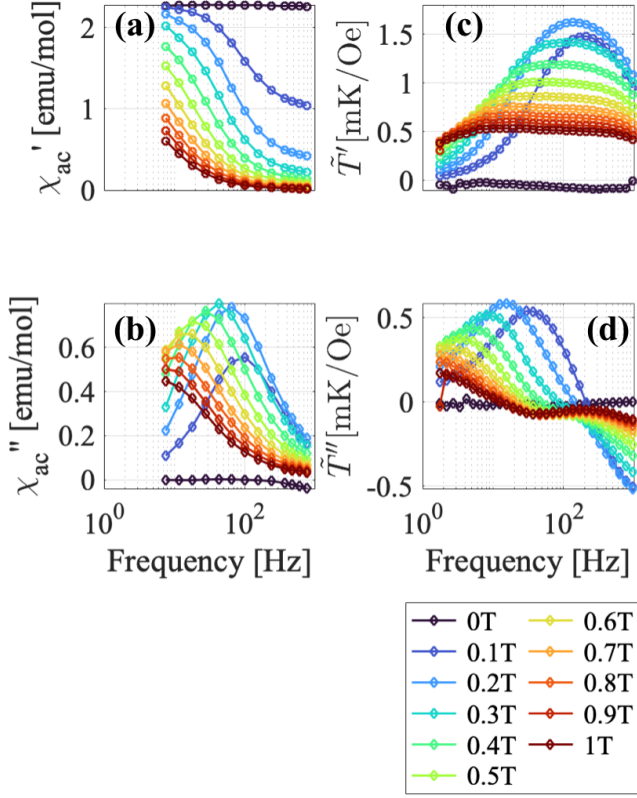


FIG. 3. Experimental results for YbVO₄ showing the frequency dependence of the real (χ'_{ac}) and imaginary (χ''_{ac}) parts of (a,b) χ^{ac} and (c,d) the AC MCE (\tilde{T}) at 3 K. Data are shown for representative DC magnetic fields from 0 T to 1 T.

of the MCE is found to occur at a frequency that reflects the geometric mean of the thermal relaxation times $\tau_{4f} = \frac{C^{4f}}{\kappa_l}$ and $\tau_{ext} = \frac{C^{4f}}{\kappa_b}$ [23], reinforcing the points made in previous sections that external relaxation effects can seriously complicate analysis of AC measurements.

VI. Results of χ^{ac} and AC MCE experiments

Fig. 3 shows the measured frequency-dependence of χ^{ac} and the AC MCE of YbVO₄ at 3 K for magnetic fields between 0 and 1 T. An AC field of 3 Oe was used. In order to ensure meaningful comparison of the two measurements, the same sample, and the same mounting configuration (corresponding to the yellow configuration shown in Fig. 2), were used for both measurements.

Before performing detailed fits to the data based on the thermal model, we first note three observations that are evident simply by inspecting the data shown in Fig. 3. First, the data clearly follow the anticipated functional forms sketched in Fig. 1(c, d). Second, there is clearly a strong field dependence to both quantities, as anticipated for YbVO₄ due to Zeeman splitting of the CEF

eigenstates. And third, the field-dependence is very similar for the two quantities; i.e. the maximum in the real part of ΔT follows the same trend as the maximum in the imaginary part of χ^{ac} . The consistency in the shift of the characteristic frequency between the two measurements implies that the same internal and extrinsic heat transfer processes are being captured in both experiments.

We note that such highly frequency-dependent responses are not observed in GdVO₄ (see Appendix. D), a material for which phonon bottleneck effects are not anticipated due to the absence of CEF effects, even when it is held under similar experimental conditions (i.e. similar external thermal relaxation). Thus the relaxation effects evident in Fig. 3 point to an intrinsic slow relaxation, as anticipated for YbVO₄, with the anticipated strong field dependence.

VII. Fits to the thermal model

The data shown in Fig. 3 can be fit to the solution provided by Eq.9 and 11 to reveal the field dependence the two time constants. (i.e. the intrinsic $\tau_{4f} = \frac{C^{4f}}{\kappa_l}$ and the extrinsic thermal relaxation $\tau_{ext} = \frac{C^{4f}}{\kappa_b}$). The fits, which we describe in greater detail below, are shown in Fig. 4 (a) and (b) as dashed lines on the associated Cole-Cole plots.

To simplify the fitting procedure, four fit parameters can be defined: $B = \frac{T\gamma^2}{\kappa_l}$, $\tau_{ext} = \frac{C^{4f}}{\kappa_b}$, $\tau_{4f} = \frac{C^{4f}}{\kappa_l}$, and $\eta = \frac{C^l}{C^{4f}}$, where γ is the magnetocaloric coefficient defined in Eq 4. For simplicity, we label the plotted value as $\tilde{T}(\omega) \equiv \Delta T^{lattice}(\omega)/(-ih)$. Therefore, $\tilde{T}(\omega)$ is an intensive value for the lattice with a unit of mK/Oe. Just like we define the dynamical susceptibility in Eq.6, the dynamical thermal response is divided by a magnetic field in phase of a $\sin(\omega t)$ signal. Therefore, the pre-factor of $-i$ remains in the frequency component.

Rewriting the four fitting equations after substitution of the redefined fitting parameters to Eq.9 and 11 yields:

$$\begin{aligned} \alpha'(\omega) &= \chi_0 - \frac{B\omega^2}{\frac{1}{\tau_{4f}} + \tau_{4f}\omega^2} \\ \alpha''(\omega) &= \frac{B\omega}{1 + \tau_{4f}^2\omega^2} \end{aligned} \quad (12)$$

$$\begin{aligned} \tilde{T}'(\omega) &= \frac{\gamma B \tau_{ext} \omega (1 - \eta \tau_{4f} \tau_{ext} \omega^2)}{\tau_{4f} + \tau_{4f}(\tau_{4f}^2 + 2\tau_{4f}\tau_{ext} + (1 + \eta)^2\tau_{ext}^2)\omega^2 + \eta^2\tau_{4f}^3\tau_{ext}^2\omega^4} \\ \tilde{T}''(\omega) &= \frac{\gamma AB \tau_{ext} (\tau_{4f} + \tau_{ext}(1 + \eta))\omega^2}{\tau_{4f} + \tau_{4f}(\tau^2 + 2\tau_{4f}\tau_{ext} + (1 + \eta)^2\tau_{ext}^2)\omega^2 + \eta^2\tau_{4f}^3\tau_{ext}^2\omega^4} \end{aligned} \quad (13)$$

where the value of χ_0 in the above can be experimentally obtained from a DC susceptibility measurement.

One final aspect of the fitting procedure accounts for the presence of the thermal sensor in the MCE measurement. The observed aspect ratio of the Cole-Cole plot of the AC MCE experiment is very slightly distorted from being a perfect complete circle predicted by Eq.11. We attribute the deviation to the effect of the thermometer that is attached to the sample, which slightly changes the thermal configuration compared to that of the χ^{ac} experiment, where a sensor is not thermally attached to the sample. From experimental observations and fit results, we find that the effect of the thermometer does not significantly affect the in-phase component $\tilde{T}'(\omega)$, but does contribute a small prefactor to the out-of-phase component $\tilde{T}''(\omega)$, resulting in a negative value for the fit parameter A with magnitude slightly less than 1. A more detailed discussion of the effect of the thermal sensor, together with experimental characterization, is given in Appendix. F.

Returning to the fit results shown in Fig. 4 panels (a) and (b), dashed lines indicate the fits of α and \tilde{T} based on Eq.12 and 13. The field dependence the two time constants that are extracted from these fits are shown in panel (c). The red data points show the results for τ_{4f} when χ^{ac} and the AC MCE data are simultaneously fit by the full thermal model involving two time constants. Yellow data points show the associated τ_{ext} values from those same fits to the full thermal model. In order to confirm that the combination fitting method is valid, we also fit the χ^{ac} data separately using only Eq.12. Blue data points show the result from fitting χ^{ac} using only a single-time constant τ_{4f} . The goodness of fits in panels (a) and (b), combined with the internal consistency of the two fitting methods shown in panel (c), imply that the frequency characteristics of the two experiments capture the same energy transfer processes very well.

To further confirm that the fit result accurately describes an internal energy exchange process between the spin and lattice components, we compare the fitted value of heat capacity ratio $\eta = \frac{C^{lattice}}{C^{4f}}$ with the calculated value for a 2-level spin system and a phonon bath with T^3 dependence. The fit parameter that describes the heat capacity ratios is shown in 4 (d), and it is indeed consistent with the calculated value.

VIII. Discussion

It is instructive to consider the relation between the discretized thermal analysis method that we present above to a generalized linear response theory. When multiple variables interact with each other in a circuit, the overall relaxation behavior is characterized by a set of thermodynamic conjugate variables, which refer to pairs of “force (f_ω)” and “displacement($x_i(\omega)$)” that respond directly to each other. A change in one variable directly affects the other. The application of “forces” results in a corresponding “displacement” that characterizes the linear response function $\alpha_i(\omega)$:

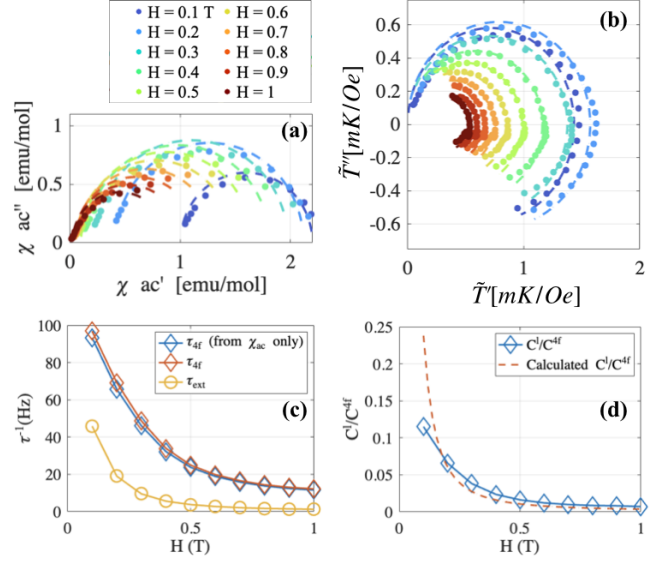


FIG. 4. Experimental determined χ^{ac} and AC MCE of YbVO₄ fitted with Eq.9 and 11. (a) A Cole-Cole plot showing the real ($\chi^{ac'}$) against the imaginary part ($\chi^{ac''}$) of the dynamical susceptibility. (b) A similar plot for the AC MCE, where $T = \Delta T$. (c) The characteristic spin-lattice relaxation time (τ_{4f} and τ_{ext}) obtained from the fits, as described in the main text. (d) The parameter C^l/C^{4f} from the fit result, compared with the calculated value based on the Schottky anomaly of the ground-state Kramers doublet in YbVO₄ and the phonon background described by the Debye Model, as described in the main text.

$$x_i(\omega) = \alpha_i(\omega)f_\omega \quad (14)$$

The most commonly existing pair of conjugate variables are temperature and entropy (T, S). When the thermodynamic state of a closed system remains unchanged by applied fields, the thermo-susceptibility is uniquely defined by the heat capacity because $\Delta S = \frac{C}{T} \Delta T$. Consequently, the dynamical response is completely determined by the rate of thermal conductance, affected by an external heat source. If, however, the system develops a caloric response, it must imply that another pair of conjugate variables exists in at least one of the circuit components. For example, the measurement results above contain 3 pairs of conjugate variables, which are (H, M) , (T^{4f}, S^{4f}) and $(T^{lattice}, S^{lattice})$. Consequently, the full relaxation behavior can be completely determined by a linear response matrix:

$$\begin{matrix} \Delta M & S^{4f} & S^{lattice} \\ -i\hbar & \alpha_{11} & \alpha_{12} & \alpha_{13} \\ T^{4f} & \alpha_{21} & \alpha_{22} & \alpha_{23} \\ T^{lattice} & \alpha_{31} & \alpha_{32} & \alpha_{33} \end{matrix} \left(\begin{matrix} \\ \\ \\ \end{matrix} \right)$$

The diagonal terms represent the susceptibility response. α_{11} is the AC magnetic susceptibility ($\alpha(\omega)$ in

Eq.2), α_{22} accounts for the thermal susceptibility of the spin affected by the magnetic field, and α_{33} accounts for thermo susceptibility of the lattice. From an experimental perspective, we note that any conventional dynamical measurement only obtains the frequency response function of the diagonal matrix element. Although all matrix elements must satisfy the relation of $\alpha_{i,i+j}\alpha_{i+j,i} = \alpha_{i,i}\alpha_{i+j,i+j}$, the matrix cannot be uniquely defined by dynamical susceptibility only. Because the term α_{33} is special in the sense that it is a single positive real constant $\frac{C^{lattice}}{T_0}$ instead of a complex response function. Therefore, the AC caloric effect function $\tilde{T}(\omega)$ can be associated with α_{13} by the relation $\tilde{T}(\omega) = \frac{\alpha_{13}}{\alpha_{33}}$.

The matrix response shown above provides an illustrative example that any dynamical behavior of a non-instantaneous magnetic response is mostly likely to be the complex result of both internal structure and extensive conditions. Hence, for systems that are composed of multiple degrees of freedom, the χ^{ac} on its own is insufficient to reflect a complete dynamical process. The discretized thermal model based on spin-lattice relaxation underscores the importance of measuring the AC caloric response as a reciprocal observation to provide complementary information to any susceptibility analysis.

IX. Summary

We have developed an experimental method to measure the AC MCE, and have introduced a discretized thermal analog circuit approach that fully describes the cross-relaxation between magnetization and temperature in the frequency domain. This approach permits a full understanding of the frequency dependence of χ^{ac} and the AC MCE.

We demonstrated the technique and the associated fitting methods using YbVO_4 , a material for which there are slow magnetic dynamics at low temperatures arising from a phonon-bottleneck effect.

The magnetic dynamics of a wide variety of materials are often inferred from just susceptibility measurements, and analysed using a Debye, or closely related, model. Associated slow dynamics can be attributed to various physical effects. While these analyses are well-motivated, they are necessarily incomplete if cross-relaxation is neglected, potentially missing or mis-characterizing important new material-specific insights. The new caloric approach developed in this paper could potentially provide additional evidence about these internal relaxation processes, while also providing a solid description of the inevitable thermal relaxation processes associated with extrinsic effects. We hope that the approach we have outlined here will prove helpful in future studies of magnetic dynamics in a wide range of materials.

X. Acknowledgements

Low-temperature measurements performed at Stanford University were supported by the Air Force Office of Scientific Research Award FA9550-24-1-0357, using a cryostat acquired with award FA9550-22-1-0084. Crystal-growth experiments were supported by the Gordon and Betty Moore Foundation Emergent Phenomena in Quantum Systems Initiative Grant GBMF9068. M.P.Z. was also partially supported by a National Science Foundation Graduate Research Fellowship under grant number DGE-1656518. L.Y. acknowledges support from Marvin Chodorow Postdoctoral Fellowship at the Department of Applied Physics, Stanford University.

Appendix A Experimental set up of the AC MCE measurement

An electronic transport measurement of a resistance bridge with a dual-frequency lock-in technique is introduced to detect and measure a temperature oscillation on the order of milliKelvins. The setup consists of the driven magnetic coil, a Stanford Research SR860 lock-in amplifier in the dual mode (measures bridge voltage V_b), and another SR860 in the external mode (measures the sample's thermometer resistance V_S). The amplified driven coil signal gives an additional isolated output via the Electronic Module of the MPMS System. The voltage output with the internal reference frequency of the first lock-in was amplified into a current signal via a Stanford Research CS580 Voltage Controlled Current Source and also gave the reference signal input of the second lock-in. The Electron Transport Option (ETO) probe provided by the MPMS accessory kits was applied to enable transport measurement.

Appendix B Energy exchange of transitions between CEF states in YbVO_4

In order to identify the transition between the magnetic induced splitting between the ground-state doublet in YbVO_4 , we consider the electron of the 4f shell embedded in a rare-earth vanadates crystal structure with D_{2d} symmetry. The corresponding CEF Hamiltonian can be written as:

$$H_{CEF} = B_2^0 O_2^0 + B_4^0 O_4^0 + B_4^4 O_4^4 + B_6^0 O_6^0 + B_6^4 O_6^4 \quad (15)$$

where B_n^m are the CEF parameters defined by the RVO_4 lattice, and O_n^m are Stevens operators. The irreducible representations of the ground-state, first and second excited states calculated for the Yb^{3+} ion with crystal field parameter [24] are:

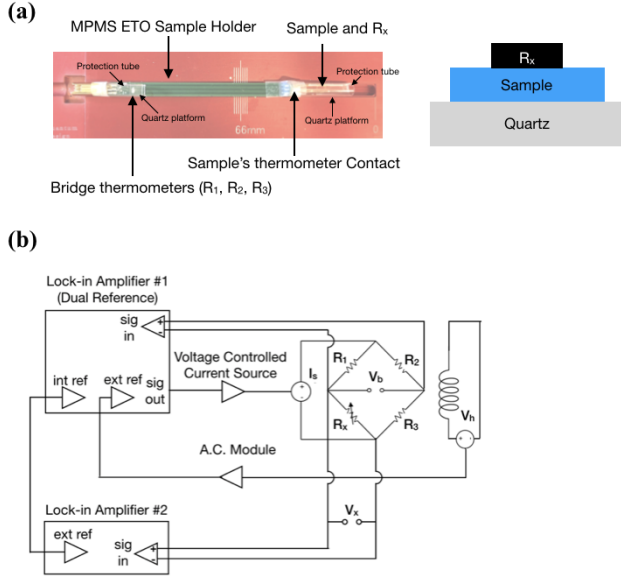


FIG. 5. (a) Actual photo of an AC MCE probe device assembly and a schematic showing the stacking sequence between thermometer R_x , sample, and the holder. The sample is located at the end quartz component that is attached to the ETO probe head. Before measurement, the center of the sample is aligned with the center of the applied magnetic field via an automatic sequence. (b) Circuit diagram of the AC MCE measurement. Here, R_x represents the thermal resistor. R_1 , R_2 , and R_3 are bridge resistors. The raw temperature oscillation signal is obtained from the bridge voltage V_b via a lock-in amplifier in a dual mode with its internal reference, and external reference from the A.C. magnetic coil (V_s). A second lock-in amplifier measures V_s to obtain the temperature profile of the thermal resistors. A Voltage Controlled Current Source converts the 1 V voltage output of the lock-in amplifier to an excitation current of 100 μ A to the Wheatstone Resistor Bridge.

$$\begin{aligned}
 \pm\Gamma_1^7 &= 0.901 \left| \pm \frac{7}{2} \right\rangle - 0.433 \left| \mp \frac{1}{2} \right\rangle, E = 0 \text{ meV} \\
 \pm\Gamma_1^6 &= \pm 0.886 \left| \pm \frac{3}{2} \right\rangle \mp 0.464 \left| \mp \frac{5}{2} \right\rangle, E = 7.2 \text{ meV} \\
 \pm\Gamma_2^7 &= 0.433 \left| \pm \frac{7}{2} \right\rangle + 0.901 \left| \mp \frac{1}{2} \right\rangle, E = 34.8 \text{ meV}
 \end{aligned} \quad (16)$$

By calculating the transitions with $\langle \Gamma | H_{CF} | \Gamma \rangle$ between the ground states and the two excited states, we found that the only transition between $(+\Gamma_1^7, +\Gamma_2^7)$ and $(-\Gamma_1^7, -\Gamma_2^7)$ are allowed, indicated by a non-zero value. Aside from crystal symmetry considerations, phonon modes investigated by room temperature Raman spectra [25, 26] and inelastic neutron scattering [24] that break the D_{2d} symmetry are being reported. Therefore, we have also taken consideration of the extra Stevens operators $\langle \Gamma | O_m^n | \Gamma \rangle$ for $m = 2, 4, 6$ and $n = 0, 2, 4, 6$ between each of the 6 total states above, we found that

the extended CEF parameters allow transition between $(+\Gamma_1^7, -\Gamma_1^6)$ and $(-\Gamma_1^7, +\Gamma_1^6)$. There is no allowed transition between the ground state doublet $\langle \Gamma_1^7 | O_m^n | -\Gamma_1^7 \rangle = 0$.

Appendix C Thermodynamic of the adiabatic magnetocaloric effects

Adiabatic condition implies that no heat exchange and the S_{4f} is conserved. Hence, we can calculate the value of γ in Eq.4 explicitly by considering the spin is subjected to the external field and is decoupled from the environment (i.e. no heat exchange to the lattice). By associating adiabatic condition with the linear response of the entropy with respect to temperature and field of the entropy, we find:

$$\begin{aligned}
 dS^{4f} &= \left(\frac{\partial S^{4f}}{\partial T} \right)_H dT + \left(\frac{\partial S^{4f}}{\partial H} \right)_T dH \\
 &= \left(\frac{C_{4f}}{T} \right) \Delta T_0 + \left(\frac{\partial S^{4f}}{\partial H} \right)_T h \\
 &= 0
 \end{aligned} \quad (17)$$

By applying the Maxwell relation $\frac{\partial S}{\partial H} = \frac{\partial M}{\partial T}$, the differential change of temperature ΔT_{ad} with respect to the excitation field h is:

$$\Delta T_{ad} = - \left(\frac{\partial M}{\partial T} \right) \frac{T}{C_{4f}} h = -\gamma_{ad} \frac{T}{C_{4f}} h \quad (18)$$

where γ_{ad} is defined as the adiabatic magnetocaloric coefficient. Eq.18 implies that AC MCE temperature oscillation ΔT_{ad} is uniquely defined by the entropy of the magnetic ions and no time constant can be associated with the thermally insulated condition. In a real experiment setup, however, the measured temperature oscillation will be different due to an extrinsic heat flow rate between the measured system and the environment, which continuously shifts between the isothermal condition at low frequency to the adiabatic condition at high frequency. In the following sections, we present a method to characterize the quasi-adiabatic regime by comparing the value of measured $\Delta T^{4f}(\omega)$, χ^{ac} to a real experimental scenario.

Appendix D χ^{ac} and AC MCE of GdVO₄

Both YbVO₄ and GdVO₄ exhibit a large magnetocaloric effect at low temperatures. Compared with YbVO₄, no magnetic relaxation effect is observed in GdVO₄ at low temperatures. Fig. 6 illustrates the calculated entropy landscapes for both compounds. These landscapes are characterized by a phonon background and rare-earth degree of freedom, exhibiting comparable temperature changes when referenced at 2K and 0T.

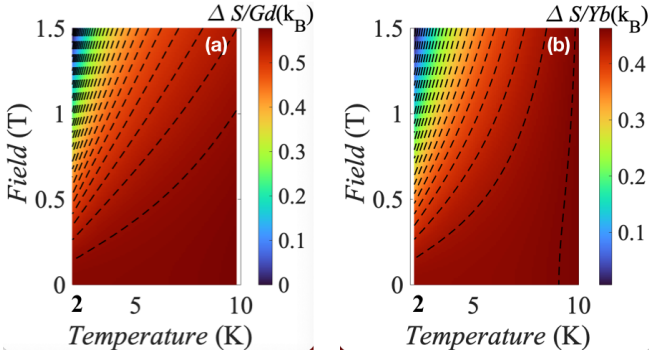


FIG. 6. The calculated entropy change of (a) GdVO₄ and (b) YbVO₄ with respect to the entropy value of 2 K and 0 T considered the total entropy of the lattice and the $4f$ contribution. The dashed lines represent isentropic contours.

Gd³⁺ ion in GdVO₄ does not split and remains an octuplet at low temperature. GdVO₄ undergoes an antiferromagnetic transition at 2.5K, followed by a Spin-flop phase down to 1.37 K [27]. Consequently, GdVO₄ will experience much less effect of such indirect transition due to much less magnetic anisotropy and very close Zeeman splitting between the CEF states. In Fig. 7, (a,b) we show the χ^{ac} at 3 K. The external magnetic field is composed of a time-independent field and an AC excitation field. χ^{ac} is plotted in the in-phase (a) and out-of-phase (b) components denoted as $\chi^{ac} = \chi' + i\chi''$. Notably, no significant frequency dependence was observed within the frequency range below 1 T, and the amplitude of the out-of-phase component remained comparable to the background noise for frequencies below 100 Hz during the measurements. The result implies an example that extrinsic time constants from both measurements lie outside the accessible frequency range of the AC experiments, as an illustrative example of a material in the absence of internal dynamics.

Appendix E Comparison with thermal conductivity measurements

The fitting of χ^{ac} in the main text assumes that the lattice is well equilibrated with the sample holder, resulting in uniform temperature spatial distributions and a time constant τ_{ext} much smaller than the spin-lattice relaxation rate. This section confirms that the sample geometry and heat diffusion constant of rare-earth vanadates support the assumption with experimental data.

For the reason of limited data availability, we take an example of thermal properties of TmVO₄ to estimate the characteristic time associated with the thermal diffusion constant in the same sample geometry as the "single-side" case in Fig. 1 (a). The thickness of the sample l is 0.1 mm. The numeric values calculated in this section are all rough estimations and cannot be applied as a ref-

erence for accurate calculation. According to Ref. [28] and Ref. [29], the thermal conductivity of TmVO₄ is close to the value of $\kappa = 0.35$ w/K² m, and keeps almost unchanged up to the higher field. and the volume heat capacity is close to the value of 0.4 J/mol K at 3 K, 0 T. Such value will be increased to roughly 2.9 J/mol K at 3 K, 1 T. By calculating the diffusion constant $D = \frac{\kappa}{C_p \rho l}$, and the characteristic frequency $f = \frac{D}{l^2}$, the extrinsic time constant is $1.3 \cdot 10^4$ Hz at a field close to zero, and $1.7 \cdot 10^3$ Hz at 1 T. This value is a few orders of magnitude larger than the internal frequency observed in the magnetic relaxation measurements.

Appendix F Effect of thermometer and mounting condition in the AC MCE experiment

To develop a generalized description of the thermometer as a discretized component, we consider the simplest scenario: A thermometer is attached to a part of a sample with thermal conductivity κ_θ . Under the same fully discretized description that assumes the sample heats uniformly with a thermometer, the temperature of the sample and thermometer are defined as $T^s(\omega)$ and $T^\theta(\omega)$. The thermal conductivity between sample/thermometer and sample/bath are κ_l and κ_b . According to the thermal transfer process between the top two components, the relation between $T^s(t)$ and $T^\theta(t)$ must satisfy:

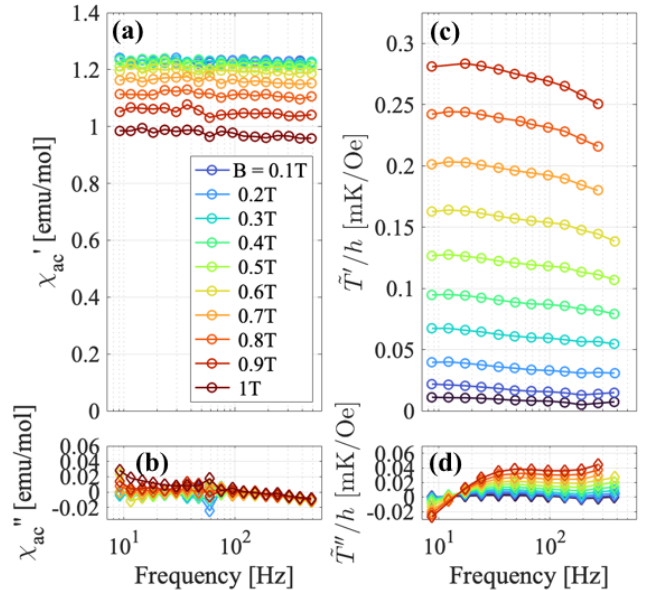


FIG. 7. (a,b) Real and imaginary part of the AC susceptibility of GdVO₄. Frequency-dependent results are plotted under different DC magnetic fields from 0 T to 0.18 T. (c,d) DC magnetic field dependence of the AC MCE effect under the same field, frequency, and AC amplitude as (a,b).

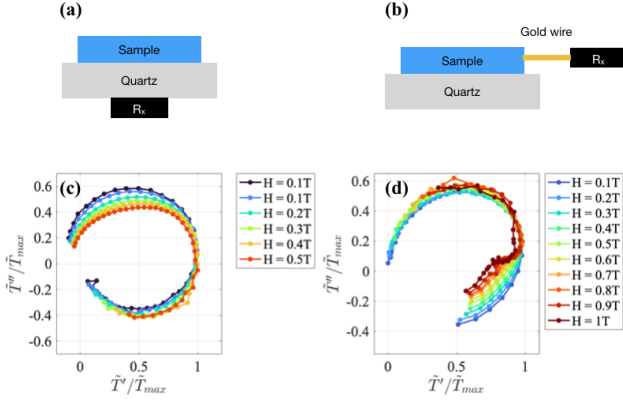


FIG. 8. (a,b) Schematics showing two additional sample mounting methods of AC MCE setup, as examples of sub-optimal mounting conditions which limited the thermo-conduction rate between samples and thermometers. In (a), the thermometer and sample are separated by the quartz component, and in (b), they are separated by a 0.05 mm diameter gold wire served as a thermal lead. (c) The Cole-Cole plot of the measurement result of the mounted method in (a). (d) The Cole-Cole plot of the measurement result of the mounted method in (b).

$$\frac{dQ(t)}{dt} = -\frac{d}{dt}S^\theta(t) = -\kappa_\theta(T^\theta(t) - T^s(t)) \quad (19)$$

when the steady-state change of entropy is periodic in both components, we can also write the equation in its frequency components:

$$\begin{aligned} -i\omega \frac{C^\theta}{T_0} T^\theta(\omega) &= -\kappa_\theta(T^\theta(\omega) - T^s(\omega)) \\ S^s(\omega) &= \frac{C^s}{T_0} T^s(\omega) \\ S^\theta(\omega) &= \frac{C^\theta}{T_0} T^\theta(\omega) \end{aligned} \quad (20)$$

The solution can be written in a matrix form as:

$$\begin{pmatrix} T^s \\ T^\theta \end{pmatrix} \begin{pmatrix} \frac{C^s}{T_0} & -\frac{C^\theta}{T_0} \frac{\kappa_\theta}{\kappa_\theta - iC^\theta\omega} \\ -\frac{C^s}{T_0} \frac{2\kappa_\theta}{\kappa_\theta + iC^\theta\omega} & \frac{C^\theta}{T_0} \end{pmatrix} \begin{pmatrix} S^s \\ S^\theta \end{pmatrix}$$

It is evident that the two off-diagonal terms have factors that are complex conjugate to each other, with their

product equal to that of the two diagonal terms. This is because the complex relaxation functions have exactly the same time constant, ensuring that their product matches the product of the diagonal term, in accordance with the defining properties of the linear response matrix. It implies that when a circuit representing a thermometer is connected to a measured species, the sign of the imaginary part of the thermometer is inverted due to a conjugate relationship.

Mathematically, Eq. 20 can be solved together with Eq. 10 by treating $T^s(\omega)$ as $T^l(\omega)$, so that the experimentally obtained AC MCE oscillations will be interpreted as $T^\theta(\omega)$. The heat flow in the real experiment may have a subtle difference from a fully discretized description. Since the size of the thermometer is much smaller than the sample, it cannot exchange heat evenly across the entire sample. Consequently, such consideration has a negligible effect when the sensor is in fairly good thermal contact with the sample. When the thermometer has a limited rate of thermal exchange defined by either geometry or contact materials, the mounting geometry effect starts to affect the thermal transfer behavior of the MCE and cannot be properly described by an ideal discretized thermal model of 2 discretized components.

To experimentally demonstrate the limited thermometer geometry effect above, we designed two experiments for comparison, where the sensor is connected indirectly to the sample. The deviation from a single circular feature shown in Fig. 4(b) is easy to obtain once the thermometer is in loose contact with the measured sample, resulting in an additional characteristic time constant aside from the two described in Eq.13. Shown in Fig. 8(a), when the sensor and the sample are separated by a single quartz component, an additional thermal time constant appears on the lower frequency side, indicated by a deviation of a circular feature on the Cole-Cole plot. Similarly, a third time constant emerges from the higher frequency side when the sample and the sensor are separated by a thermal lead component, such as a thin gold wire in between. In summary, the thermometer effect can be addressed by observing an additional time constant from the measurement by a Cole-Cole analysis. A sample in the absence of spin-lattice relaxation, such as GdVO_4 , will be helpful for experimentalists to calibrate the probe geometry design and optimize the thermal mounting condition. Despite a reduction of the out-of-phase component, the optimized mounting recipe shown in the main text is important to obtain the intrinsic relaxation effect in YbVO_4 that is consistent with the χ^{ac} measurement.

-
- [1] C. V. Topping and S. J. Blundell, *Journal of Physics: Condensed Matter* **31**, 013001 (2018).
 [2] J. K. Krause, V. Wang, and B. C. Dodrill, “Magnetic property characterization system employing a single sens-

ing coil arrangement to measure ac susceptibility and dc moment of a sample,” (U.S. Patent 5 311 125, May, 1994).

- [3] K. Fischer and J. Hertz, *Spin Glasses*, Cambridge Studies in Magnetism (Cambridge University Press, 1993).
- [4] S. Gómez-Coca, A. Urtizberea, E. Cremades, P. J. Alonso, A. Camón, E. Ruiz, and F. Luis, *Nature Communications* **5**, 4300 (2014).
- [5] Y. Tang, “Heat transfer and thermal analysis with computational fluid dynamics,” (IntechOpen, Rijeka, 2024).
- [6] R. Iguchi, D. Fukuda, J. Kano, T. Teranishi, and K.-i. Uchida, *Applied Physics Letters* **122**, 082903 (2023).
- [7] E. Warburg, *Annalen der Physik* **249**, 141 (1881).
- [8] Y. Kohama, C. Marcenat, T. Klein, and M. Jaime, *Review of Scientific Instruments* **81**, 104902 (2010).
- [9] E. Brück, *Journal of Physics D: Applied Physics* **38**, R381 (2005).
- [10] J. Y. Law, V. Franco, L. M. Moreno-Ramírez, A. Conde, D. Y. Karpenkov, I. Radulov, K. P. Skokov, and O. Gutfleisch, *Nature Communications* **9**, 2680 (2018).
- [11] C. Pereira, R. Almeida, R. Kiefe, C. Amorim, D. Silva, J. Amaral, and J. Belo, *Journal of Alloys and Compounds* **976**, 173290 (2024).
- [12] B. Fischer, J. Hoffmann, H. Kahle, and W. Paul, *Journal of Magnetism and Magnetic Materials* **94**, 79 (1991).
- [13] Y. Tokiwa and P. Gegenwart, *Review of Scientific Instruments* **82**, 013905 (2011).
- [14] A. Aliev, A. Batdalov, L. Khanov, V. Koledov, V. Shavrov, I. Tereshina, and S. Taskaev, *Journal of Alloys and Compounds* **676**, 601 (2016).
- [15] *Journal of Magnetism and Magnetic Materials* **553**, 169300 (2022).
- [16] P. Radhakrishna, J. Hammann, and P. Pari, *Journal of Magnetism and Magnetic Materials* **23**, 254 (1981).
- [17] Z. A. Kazei and R. I. Chanieva, *Journal of Experimental and Theoretical Physics* **102**, 266 (2006).
- [18] E. Palacios, M. Evangelisti, R. Sáez-Puche, A. J. Dos Santos-García, F. Fernández-Martínez, C. Cascales, M. Castro, R. Burriel, O. Fabelo, and J. A. Rodríguez-Velamazán, *Phys. Rev. B* **97**, 214401 (2018).
- [19] R. Orbach, *Proceedings of the Royal Society of London. Series A, Mathematical and Physical Sciences* **264**, 458 (1961).
- [20] R. Feigelson, *Journal of the American Ceramic Society* **51**, 538 (1968).
- [21] S. Smith and B. Wanklyn, *Journal of Crystal Growth* **21**, 23 (1974).
- [22] K. Oka, H. Unoki, H. Shibata, and H. Eisaki, *Journal of crystal growth* **286**, 288 (2006).
- [23] In principle, we can also use $C^{lattice}$ to define the τ_{ext} . We eventually chose to use C^{4f} instead of $C^{lattice}$ for simplicity during fitting analysis.
- [24] J. Nipko, C.-K. Loong, S. Kern, M. Abraham, and L. Boatner, *Journal of Alloys and Compounds* **250**, 569 (1997).
- [25] C. C. Santos, E. N. Silva, A. P. Ayala, I. Guedes, P. S. Pizani, C.-K. Loong, and L. A. Boatner, *Journal of Applied Physics* **101**, 053511 (2007).
- [26] C. Santos, I. Guedes, C.-K. Loong, and L. Boatner, *Vibrational Spectroscopy* **45**, 95 (2007), raman Spectroscopy Workshop 2006.
- [27] B. W. Mangum and D. D. Thornton, *AIP Conference Proceedings* **5**, 311 (1972).
- [28] P. Massat, J. Wen, J. M. Jiang, A. T. Hristov, Y. Liu, R. W. Smaha, R. S. Feigelson, Y. S. Lee, R. M. Fernandes, and I. R. Fisher, *Proceedings of the National Academy of Sciences* **119**, e2119942119 (2022).
- [29] A. Vallipuram, L. Chen, E. Campillo, M. Mezidi, G. Grissonnanche, M.-E. Boulanger, E. Lefrançois, M. P. Zic, Y. Li, I. R. Fisher, J. Baglo, and L. Taillefer, *Phys. Rev. B* **110**, 045144 (2024).